

Supplementary Materials for
Electrically addressable integrated intelligent terahertz metasurface

Benwen Chen *et al.*

Corresponding author: Jinbo Wu, jbwu@nju.edu.cn; Biaobing Jin, bbjin@nju.edu.cn

Sci. Adv. **8**, eadd1296 (2022)
DOI: 10.1126/sciadv.add1296

The PDF file includes:

Sections S1 to S7
Figs. S1 to S6
Legends for movies S1 and S2
References

Other Supplementary Material for this manuscript includes the following:

Movies S1 and S2

Section S1: Device fabrication and assembly process

The device fabrication process is listed as follows.

- (1) VO₂ film deposition on the sapphire substrate
- (2) Photoresist spin coating and patterning using ultraviolet photolithography
- (3) Etching VO₂ film by reactive ion etching
- (4) Radio frequency sputtering of titanium and gold films on the bottom surface of the substrate
- (5) Photoresist spin coating and patterning using ultraviolet photolithography
- (6) Radio frequency sputtering of titanium and gold films and lift-off process
- (7) Assembling the device on the printed circuit board and wire bonding

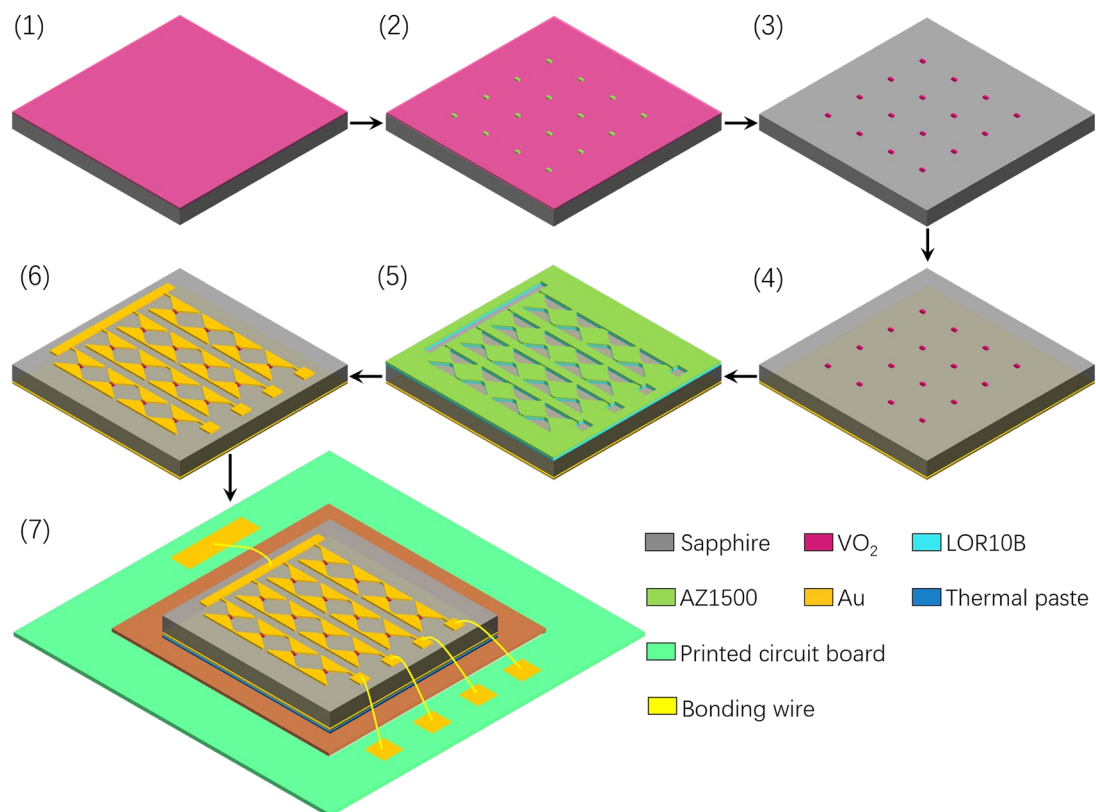


Fig. S1. Flow chart of the device fabrication and assembly process.

Section S2: Optimization of the electrical connection between different unit cells in the subarray for THz wave detection

When one subarray of the SAM is chosen as a THz sensor, the unit cells in this subarray ideally should be connected in series so that the output voltage of the subarray is their sum. However, it will make the total resistance of the subarray (R_{sub}) relatively large. Then, the input power of the subarray (P_{in}) would be insufficient to trigger the insulator-metal-transition (IMT) of VO₂ according to the relationship $P_{\text{in}} = V_{\text{out}}^2/R_{\text{sub}}$, where V_{out} is limited by the maximum output voltage of the 48-channel power amplifier. Hence, the optimization of the electrical connection of the unit cells is indispensable.

As discussed in the main text, each subarray comprises 90 rows and 2 columns of unit cells.

For simplicity, the connection layout of the unit cells in these two columns is identical. R_{col} denotes the column resistance, and these two columns are in parallel to reduce R_{sub} , which can be described as $R_{\text{sub}} = R_{\text{col}} / 2$. To further reduce R_{col} without significantly sacrificing THz-detection capability, the optimized design of the electric connection in each column is shown in Fig. S2A. The column is divided into nine identical blocks in series connection. Thus, $R_{\text{col}} = 9R_{\text{block}}$, where R_{block} is the resistance of a block. There are 10 unit cells in parallel in each block, and the block resistance $R_{\text{block}} = R_{\text{u}} / 10$, where R_{u} is the resistance of a unit cell. R_{u} depends on the VO₂ conductivity because the length-width ratio and the thickness of the VO₂ patch are fixed. Eventually, R_{sub} is optimized as $R_{\text{sub}} = 9R_{\text{u}} / 20$, as shown in Fig. S2B.

The above optimization is subject to the limited voltage of the 48-channel power amplifier, and the THz-detection capability is partly sacrificed. If a power supply with a larger output voltage is exclusively applied to a subarray, optimizing the electrical connection between the unit cells in this subarray could prioritize the detection capability. Hence, in our SAM, we design the electrical connection in the 24th subarray (at the center of the SAM) with the connection layout shown in Fig. S2C, in which more unit cells are in series, which improves the output voltage. In this case, the total resistance of the subarray is $R_{\text{sub}} = 45R_{\text{u}}/4$, and the bias of the subarray is supplied by a voltage source (Keithley SMU2400) instead of the power amplifier.

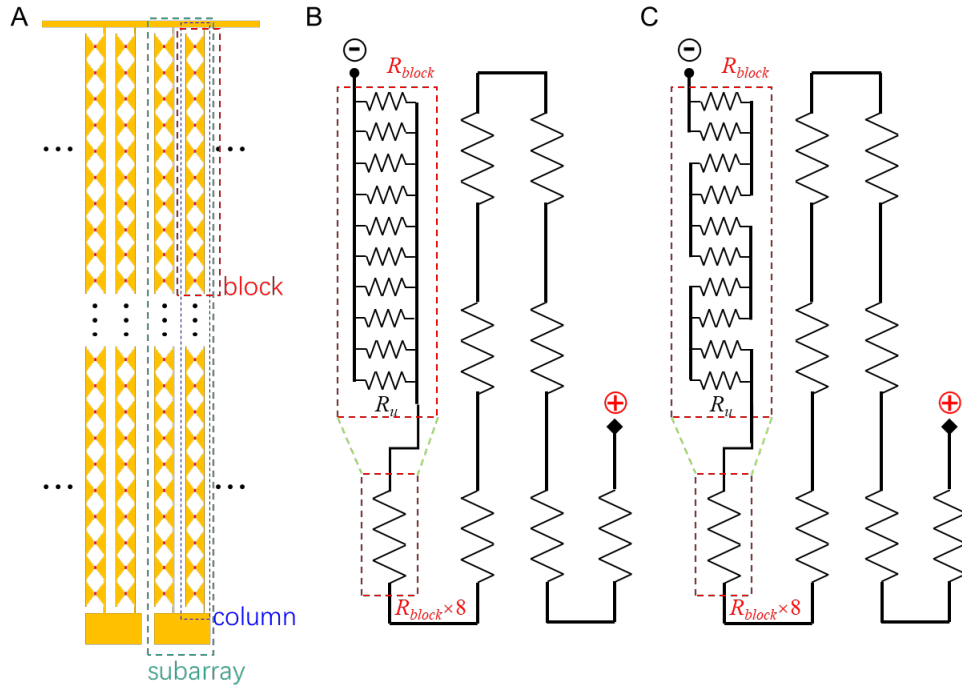


Fig. S2. Resistance of the subarray, column, and block. (A) Schematic of two subarrays in the proposed linear array. (B) Equivalent resistance model of a column in each subarray, except for the 24th subarray. (C) An equivalent resistance model of the column in the 24th subarray for improving THz wave detection.

Section S3: THz detection performance of the modulation subarrays in the SAM.

As discussed above, when optimizing the electrical connections between unit cells in the subarray, there is a contradiction between increasing the THz detection capability and reducing R_{sub} . For sensor subarray, the relatively high R_{sub} is necessary to improve the detection sensitivity. In contrast, the unit cell connections in modulation subarrays were optimized in the opposite direction. Nonetheless, these subarrays were still capable of detecting THz waves. For verification, we used these subarrays to measure the power distribution of a collimated THz beam impinging on the SAM, as illustrated in Fig. S3A. The THz radiation with a modulation frequency (f_{mod}) of 3.1 kHz is collimated and incident to the SAM, which was biased at 60°C. The subarrays in the SAM are biased with a current of 4 mA for THz detection, and the voltage across each subarray is sent to the lock-in amplifier (MFLI, Zurich Instruments) for demodulation. The readout value of each subarray is shown in Fig. S3B. Because of the Gaussian distribution of the power of the collimated THz beam, the subarrays at the edge of the incident spot did not detect any THz power; Fig. S3B only shows the readout values of those subarrays that are in the middle of the spot. Figure S3B proves that although the 24th subarray performed much better than the others in terms of responsivity, the other subarrays could still work as THz sensors, indicating that the proposed SAM could also be used as a linear sensor array.

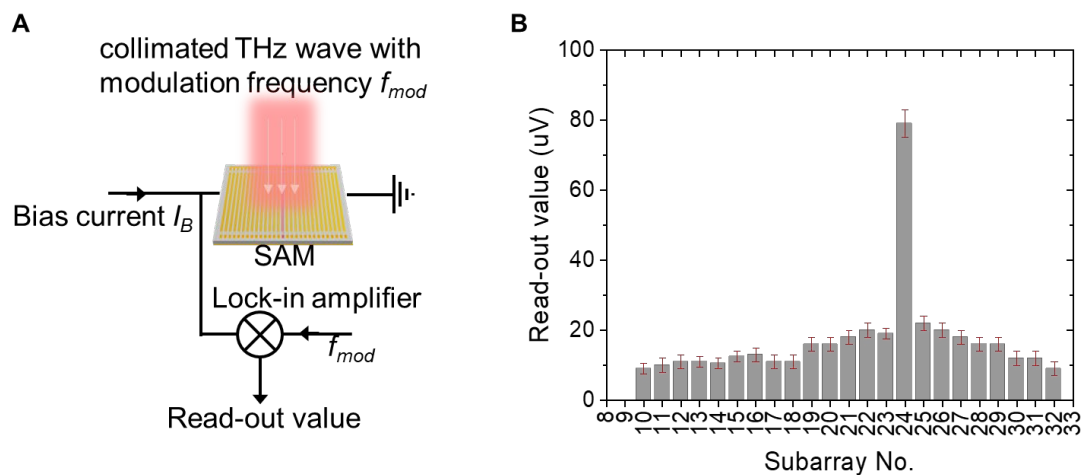


Fig. S3. Characterization of the subarrays in the SAM for THz detection. (A) Schematic of the setup used to characterize the subarrays. (B) The detected value of each subarray at a modulation frequency of 3.1 kHz and a 4-mA DC bias.

Section S4: Experimental setup used for the two proof-of-concept demonstrations.

To prove the capability of the proposed SAM in the application scenarios such as self-adaptive beam steering and THz power stabilization, the experimental setup for the two demonstrations was established. The real experimental setup and the diagram are shown in Fig. S4.

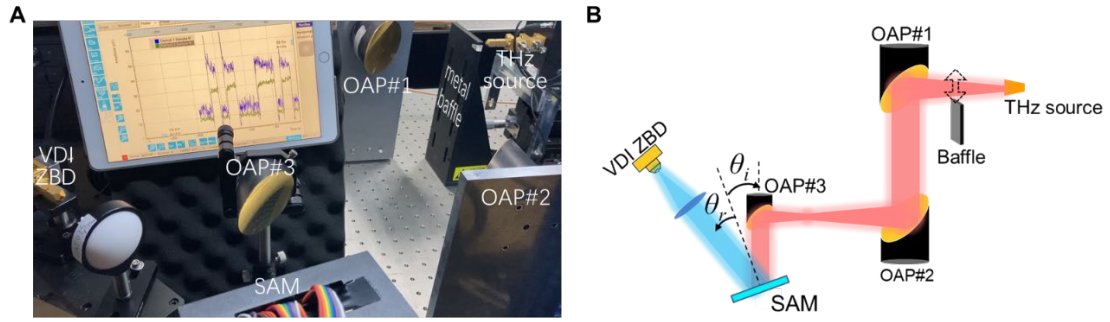


Fig. S4. Experimental setup used for the demonstrations. (A) The optical image of the setup. (B) Schematic of this experimental setup.

Section S5: Review of THz phase modulators and detectors.

Phase modulators in the THz band are far from mature compared with microwave frequencies. The phased array technology is widely used at microwave frequencies, while its development at THz frequencies encounters many technical challenges. The low performance and complicated fabrication process of the semiconductor lumped components in the THz region are the major problems. One solution is to modulate the phase in the lower frequency band and then convert it to the THz region. For example, Yang *et al.* proposed a phased array composed of eight elements in the frequency range of 360-420 GHz using 45 nm CMOS (complementary metal-oxide-semiconductor) silicon on insulator technology (53). Another way of tuning the phase shift in the THz band is realized based on Adler's equations, which have been reported in the recent literature (54-55).

The high hardware complexity of the active phased arrays limits their array size and brings unaffordable costs. There are some alternatives proposed to realize phase modulation. Leaky-wave antenna, which has frequency scanning capability, is a popular choice for THz beam steering. The phase shift in the traveling waveguide structure is obtained by adjusting the spacing between the inter elements. The leaky-wave antenna has been demonstrated to use in the THz radar and wireless communication (56-58). Its major drawback is lacking the reconfigurability. Recently, the tunable Brewster effect has been utilized to realize broadband phase modulation (59). The reconfigurable and frequency dispersive THz beam deflection has been experimentally demonstrated (60).

The metasurface-based passive phased array, i.e., reflective intelligent surface (RIS), was proposed in recent years. It integrates with tunable materials to realize the dynamic control of the phase. Here, the word "passive" denotes it does not contain the THz source. It owns the advantages

of simple geometry and simple fabrication process in contrast to the transmitter-based active phased array, which is favorable for reducing the fabrication cost. Recently, programmable metasurfaces based on liquid crystal and graphene have been proposed to realize THz beam steering (27,29,31).

The function of the THz detector is to receive the THz radiation signal and convert it to physical quantities that humans can understand. To meet the application requirements of THz technology in biomedical imaging, astronomical observation, security detection, and other fields, high-performance and low-cost detectors are highly required. Generally, the THz detector can be divided into direct and coherent detectors. Though the coherent detector has the capability of frequency resolution, it is challenging to fabricate large-scale arrays as it requires the local oscillator as the reference. The direct detector has a simple structure and low cost, so it is very suitable for large-scale imaging arrays.

Based on the physical mechanism of direct detectors, it can be divided into the following categories: the thermal detectors essentially measure the energy released by the incident THz photons via the change in thermometric properties in various materials, and typical thermal detectors include Golay cell, pyroelectric detector, and bolometer; the plasmonic detectors measure the THz signals utilizing the interaction between THz radiation and collective motion of electrons in the field effect transistor; “electronic” detectors such as Schottky barrier diode, resonant tunneling diode represent the detectors using the THz radiation to induce the electron transition.

Among the various direct detectors, the thermal detectors have the lowest cost compared with other detectors (33). In this work, the THz detection capability is realized using the high-temperature coefficient of resistance (TCR) of the VO₂ film. It belongs to the microbolometer, one of the most widely used thermal detectors. In recent years, microbolometers have been commercialized, and the array size has reached tens of kilo-pixels.

Section S6. Discussion on extending the integrated self-adaptive metasurface to other tunable materials and electromagnetic frequency bands.

We claimed that our work could be transferred to other tunable materials and frequency bands in the main text. Here we would like to discuss the feasibility further.

The plasmonic effect in field-effect transistors (FET) such as GaN and GaAs high electron mobility transistor, CMOS FET, have been utilized for sensitive THz detection and modulation (61-

66). The concept of self-adaptive metasurface with the detection and modulation functions is potentially realized using the semiconductor FETs at THz frequencies.

The self-adaptive metasurface based on phase change material (PCM) is feasible in the infrared band. PCM is widely used as the infrared microbolometer because of the large temperature coefficient of resistance (TCR). (67-68) . Chen *et al.* designed and fabricated a 32×32 VO₂-based infrared detector array with the implantation of the required CMOS readout electronics (69). In addition to the superior detection capability, some recent work demonstrates the modulation capability of PCM (70, 71). For example, an electrically tunable reflectarray metasurface capable of continuously modulating the phase of reflected light in the near-infrared regime is recently reported (71). Based on the above analysis, we believe PCM is a good material choice for electrically addressable self-adaptive metasurface with detection and modulation capabilities in the infrared band.

Graphene and other two-dimensional materials are candidates for self-adaptive metasurfaces in a broad spectrum. Graphene and other two-dimensional materials have been used as photodetectors in a broad spectrum range from THz to ultraviolet light (72). In addition to the bolometric mechanism, there are a variety of other mechanisms for two-dimensional materials to achieve highly-sensitive detection. On the other hand, Ergoktas *et al.* recently demonstrated that graphene-based surface devices could be used to realize broadband modulation from microwave to visible spectrum (73). Moreover, the thermal crosstalk between adjacent pixels for two-dimensional materials is negligible because of their low energy consumption for state switching. Therefore, the concept of self-adaptive metasurface can be transferred to graphene and other two-dimensional materials. The working spectrum can be extended from THz to optical bands.

Section S7. Electromagnetic and thermal analysis of the SAM

To study the electromagnetic response of the SAM when the conductivity of VO₂ films changes, we simulated the reflection spectra of the unit cell. In the simulation, the sapphire substrate has a relative permittivity $\epsilon_{\text{sub}} = 9.4 + 0.0376i$, and gold is taken as a lossy metal with a conductivity of 4.561×10^7 S/m. The conductivity of VO₂ films in the simulation is 6×10^3 , 4×10^4 , and 2.5×10^5 S/m for the OFF, IM and ON states, respectively. The unit cell is incident with a plane wave along the z direction, and the periodic boundary conditions are applied in the x - and y - directions. The simulated

reflection spectra are fitted and analyzed based on transmission line theory, which is similar to the previous work (24).

To analyze the thermal crosstalk using a thermal paste, we used COMSOL Multiphysics to simulate the temperature distribution. Figure S5 shows the thermal model used in the simulation. The thermal paste is filled between the metasurface and the hot plate, and the temperature of the hot plate is fixed at 60°C as it can be treated as a heat sink. The boundary condition at the surfaces exposed to the air is described with convective heat flux (q_0). It is calculated as $q_0 = h (T - T_{\text{air}})$, where h is the heat transfer coefficient, and T_{air} is the ambient temperature. In the simulation, $h = 20 \text{ W m}^{-2}\text{K}^{-1}$ and $T_{\text{air}} = 25^\circ\text{C}$. For simplicity, the bowtie antennas and VO₂ patches in the triggered subarrays are fixed at 68°C, while the initial temperature of other subarrays is 60°C. The thermal conductivity, specific heat capacity, and mass density of VO₂ were $6.8 \text{ W m}^{-1}\text{K}^{-1}$, $690 \text{ J kg}^{-1}\text{K}^{-1}$, and 4340 kg m^{-3} . Other properties of materials, including the sapphire substrate and gold, can be found in Table 1 of Ref. 24.

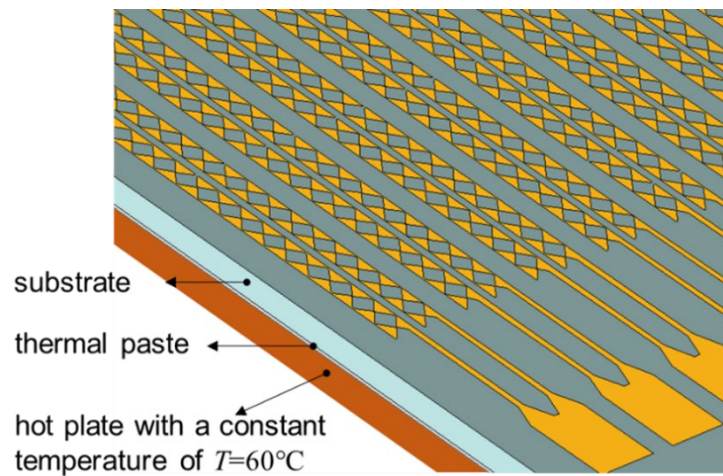


Fig. S5. Thermal model used for the numerical simulation of the thermal crosstalk.

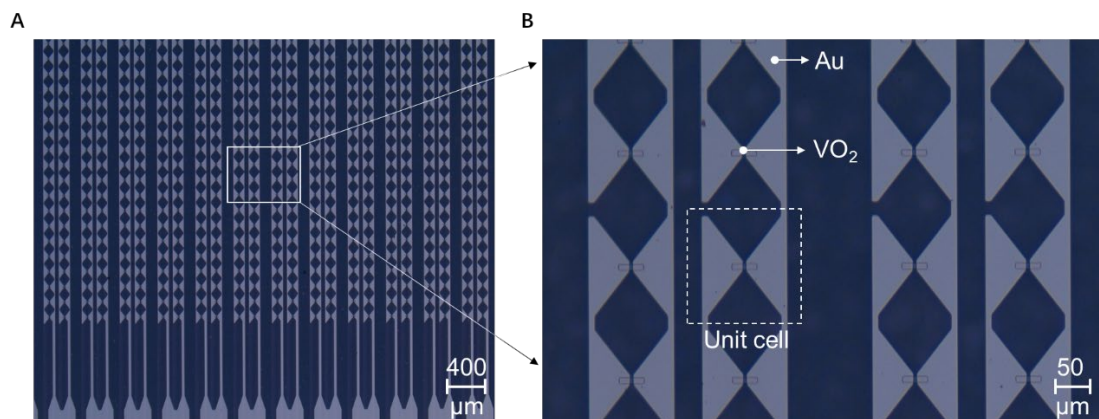


Fig. S6. Microscopic image of the fabricated device. (A) Microscopic image and (B) the close-up of the top layer of the fabricated device.

Supplementary Movie S1

A movie record of the self-adaptive THz beam deflection of the proposed SAM with the predefined software, corresponding to the first demonstration in the main text.

Supplementary Movie S2

A movie record of the performance of the SAM in maintaining power stability despite incident power fluctuation, corresponding to the second demonstration in the main text.

REFERENCES AND NOTES

1. T. Nagatsuma, G. Ducournau, C. C. Renaud, Advances in terahertz communications accelerated by photonics. *Nat. Photonics* **10**, 371–379 (2016).
2. S. Dang, O. Amin, B. Shihada, M.-S. Alouini, What should 6G be? *Nat. Electron.* **3**, 20–29 (2020).
3. S. Ummethala, T. Harter, K. Koehnle, Z. Li, S. Muehlbrandt, Y. Kutuvantavida, J. Kemal, P. Marin-Palomo, J. Schaefer, A. Tessmann, S. K. Garlapati, A. Bacher, L. Hahn, M. Walther, T. Zwick, S. Randel, W. Freude, C. Koos, THz-to-optical conversion in wireless communications using an ultra-broadband plasmonic modulator. *Nat. Photonics* **13**, 519–524 (2019).
4. S. Hu, F. Rusek, O. Edfors, Beyond massive MIMO: The potential of data transmission with large intelligent surfaces. *IEEE Trans. Signal Process.* **66**, 2746–2758 (2018).
5. C. Huang, A. Zappone, G. C. Alexandropoulos, M. Debbah, C. Yuen, Reconfigurable intelligent surfaces for energy efficiency in wireless communication. *IEEE Trans. Wireless Commun.* **18**, 4157–4170 (2019).
6. M. D. Renzo, A. Zappone, M. Debbah, M. S. Alouini, C. Yuen, J. D. Rosny, S. Tretyakov, Smart radio environments empowered by reconfigurable intelligent surfaces: How it works, state of research, and the road ahead. *IEEE J. Sel. Areas Commun.* **38**, 2450–2525 (2020).
7. L. Zhang, M. Z. Chen, W. Tang, J. Y. Dai, L. Miao, X. Y. Zhou, S. Jin, Q. Cheng, T. J. Cui, A wireless communication scheme based on space- and frequency-division multiplexing using digital metasurfaces. *Nat. Electron.* **4**, 218–227 (2021).
8. T. J. Cui, M. Q. Qi, X. Wan, J. Zhao, Q. Cheng, Coding metamaterials, digital metamaterials and programmable metamaterials. *Light Sci. Appl.* **3**, e218 (2014).
9. F. Liu, A. Ptilakis, M. S. Mirmoosa, O. Tsilipakos, X. Wang, A. C. Tasolamprou, S. Abadal, A. Cabellos-Aparicio, E. Alarcón, C. Liaskos, N. V. Kantartzis, M. Kafesaki, E. N. Economou, C. M. Soukoulis, S.

Tretyakov, Programmable Metasurfaces: State of the Art and Prospects, in *2018 IEEE International Symposium on Circuits and Systems (ISCAS)* (2018) pp. 1–5.

10. L. Li, H. Zhao, C. Liu, L. Li, T. J. Cui, Intelligent metasurfaces: Control, communication and computing. *eLight* **2**, 7 (2022).
11. R. Zhu, J. Wang, T. Qiu, Y. Han, X. Fu, Y. Shi, X. Liu, T. Liu, Z. Zhang, Z. Chu, C.-W. Qiu, S. Qu, Remotely mind-controlled metasurface via brainwaves. *eLight* **2**, 10 (2022).
12. Q. Ma, W. Gao, Q. Xiao, L. Ding, T. Gao, Y. Zhou, X. Gao, T. Yan, C. Liu, Z. Gu, X. Kong, Q. H. Abbasi, L. Li, C.-W. Qiu, Y. Li, T. J. Cui, Directly wireless communication of human minds via non-invasive brain-computer-metasurface platform. *eLight* **2**, 11 (2022).
13. Q. Ma, G. D. Bai, H. B. Jing, C. Yang, L. Li, T. J. Cui, Smart metasurface with self-adaptively reprogrammable functions. *Light: Sci. Appl.* **8**, 98 (2019).
14. C. Qian, B. Zheng, Y. Shen, L. Jing, E. Li, L. Shen, H. Chen, Deep-learning-enabled self-adaptive microwave cloak without human intervention. *Nat. Photonics* **14**, 383–390 (2020).
15. L. Li, H. Ruan, C. Liu, Y. Li, Y. Shuang, A. Alu, C. W. Qiu, T. J. Cui, Machine-learning reprogrammable metasurface imager. *Nat. Commun.* **10**, 1082 (2019).
16. M. Mercuri, I. R. Lorato, Y.-H. Liu, F. Wieringa, C. V. Hoof, T. Torfs, Vital-sign monitoring and spatial tracking of multiple people using a contactless radar-based sensor. *Nat. Electron.* **2**, 252–262 (2019).
17. H. P. Wang, Y. B. Li, H. Li, J. L. Shen, S. Y. Dong, S. Y. Wang, K. N. Qi, Q. Ma, S. Jin, S. J. Li, T. J. Cui, Intelligent metasurface with frequency recognition for adaptive manipulation of electromagnetic wave. *Nanophotonics* **11**, 1401–1411 (2022).

18. H. P. Wang, Y. X. Zhou, H. Li, G. D. Liu, S. M. Yin, P. J. Li, S. Y. Dong, C. Y. Gong, S. Y. Wang, Y. B. Li, T. J. Cui, Noncontact electromagnetic wireless recognition for prosthesis based on intelligent metasurface. *Adv. Sci.* **9**, 2105056 (2022).
19. S. Koenig, D. Lopez-Diaz, J. Antes, F. Boes, R. Henneberger, A. Leuther, A. Tessmann, R. Schmogrow, D. Hillerkuss, R. Palmer, T. Zwick, C. Koos, W. Freude, O. Ambacher, J. Leuthold, I. Kallfass, Wireless sub-THz communication system with high data rate. *Nat. Photonics* **7**, 977–981 (2013).
20. P. C. Wu, R. A. Pala, G. Kafaie Shirmanesh, W. H. Cheng, R. Sokhoyan, M. Grajower, M. Z. Alam, D. Lee, H. A. Atwater, Dynamic beam steering with all-dielectric electro-optic III-V multiple-quantum-well metasurfaces. *Nat. Commun.* **10**, 3654 (2019).
21. H. T. Chen, W. J. Padilla, M. J. Cich, A. K. Azad, R. D. Averitt, A. J. Taylor, A metamaterial solid-state terahertz phase modulator. *Nat. Photonics* **3**, 148–151 (2009).
22. Q. Wang, E. T. F. Rogers, B. Gholipour, C.-M. Wang, G. Yuan, J. Teng, N. I. Zheludev, Optically reconfigurable metasurfaces and photonic devices based on phase change materials. *Nat. Photonics* **10**, 60–65 (2016).
23. M. R. Hashemi, S. H. Yang, T. Wang, N. Sepulveda, M. Jarrahi, Electronically-controlled beam-steering through vanadium dioxide metasurfaces. *Sci. Rep.* **6**, 35439 (2016).
24. B. Chen, J. Wu, W. Li, C. Zhang, K. Fan, Q. Xue, Y. Chi, Q. Wen, B. Jin, J. Chen, P. Wu, Programmable terahertz metamaterials with non-volatile memory. *Laser Photonics Rev.* **16**, 2100472 (2022).
25. X. Duan, S. T. White, Y. Cui, F. Neubrech, Y. Gao, R. F. Haglund, N. Liu, Reconfigurable multistate optical systems enabled by VO₂ phase transitions. *ACS Photonics* **7**, 2958–2965 (2020).

26. G. Perez-Palomino, M. Barba, J. A. Encinar, R. Cahill, R. Dickie, P. Baine, M. Bain, Design and demonstration of an electronically scanned reflectarray antenna at 100 GHz using multiresonant cells based on liquid crystals. *IEEE Trans. Antennas Propag.* **63**, 3722–3727 (2015).
27. J. Wu, Z. Shen, S. Ge, B. Chen, Z. Shen, T. Wang, C. Zhang, W. Hu, K. Fan, W. Padilla, Y. Lu, B. Jin, J. Chen, P. Wu, Liquid crystal programmable metasurface for terahertz beam steering. *Appl. Phys. Lett.* **116**, 131104 (2020).
28. J. Li, P. Yu, S. Zhang, N. Liu, Electrically-controlled digital metasurface device for light projection displays. *Nat. Commun.* **11**, 3574 (2020).
29. C. X. Liu, F. Yang, X. J. Fu, J. W. Wu, L. Zhang, J. Yang, T. J. Cui, Programmable manipulations of terahertz beams by transmissive digital coding metasurfaces based on liquid crystals. *Adv. Opt. Mater.* **9**, 2100932 (2021).
30. M. A. Naveed, J. Kim, I. Javed, M. A. Ansari, J. Seong, Y. Massoud, T. Badloe, I. Kim, K. Riaz, M. Zubair, M. Q. Mehmood, J. Rho, Novel spin-decoupling strategy in liquid crystal-integrated metasurfaces for interactive metadisplays. *Adv. Opt. Mater.* **10**, 2200196 (2022).
31. M. Tamagnone, S. Capdevila, A. Lombardo, J. Wu, A. Zurutuza, A. Centeno, A. Ionescu, A. Ferrari, J. Mosig, Graphene reflectarray metasurface for terahertz beam steering and phase modulation. arXiv:1806.02202 (2018).
32. E. Carrasco, J. Perruisseau-Carrier, Reflectarray antenna at terahertz using graphene. *IEEE Antennas Wirel. Propag. Lett.* **12**, 253–256 (2013).
33. R. A. Lewis, A review of terahertz detectors. *J. Phys. D Appl. Phys.* **52**, 433001 (2019).
34. S. H. Lee, M. Choi, T.-T. Kim, S. Lee, M. Liu, X. Yin, H. K. Choi, S. S. Lee, C.-G. Choi, S.-Y. Choi, X. Zhang, B. Min, Switching terahertz waves with gate-controlled active graphene metamaterials. *Nat. Mater.* **11**, 936–941 (2012).

35. M. Mittendorff, S. Winnerl, J. Kamann, J. Eroms, D. Weiss, H. Schneider, M. Helm, Ultrafast graphene-based broadband THz detector. *Appl. Phys. Lett.* **103**, 021113 (2013).
36. M. Seo, J. Kyoung, H. Park, S. Koo, H.-s. Kim, H. Bernien, B. J. Kim, J. H. Choe, Y. H. Ahn, H.-T. Kim, N. Park, Q. H. Park, K. Ahn, D.-s. Kim, Active terahertz nanoantennas based on VO₂ phase transition. *Nano Lett.* **10**, 2064–2068 (2010).
37. C. H. Chen, X. J. Yi, X. R. Zhao, B. F. Xiong, Characterizations of VO₂-based uncooled microbolometer linear array. *Sens. Actuators A* **90**, 212–214 (2001).
38. M. S. Vitiello, D. Coquillat, L. Viti, D. Ercolani, F. Teppe, A. Pitanti, F. Beltram, L. Sorba, W. Knap, A. Tredicucci, Room-temperature terahertz detectors based on semiconductor nanowire field-effect transistors. *Nano Lett.* **12**, 96–101 (2012).
39. C. Zhang, G. Zhou, J. Wu, Y. Tang, Q. Wen, L. Shaoxian, J. Han, B. Jin, J. Chen, P. Wu, Active control of terahertz waves using vanadium-dioxide-embedded metamaterials. *Phys. Rev. Appl.* **11**, 054016 (2019).
40. A. Sharoni, J. G. Ramirez, I. K. Schuller, Multiple avalanches across the metal-insulator transition of vanadium oxide nanoscaled junctions. *Phys. Rev. Lett.* **101**, 026404 (2008).
41. R. Lu, Z. Li, G. Xu, J. Z. Wu, Suspending single-wall carbon nanotube thin film infrared bolometers on microchannels. *Appl. Phys. Lett.* **94**, 163110 (2009).
42. C. Caloz, T. Itoh, *Electromagnetic Metamaterials: Transmission Line Theory and Microwave Applications*. John Wiley & Sons (2005).
43. L. Fu, H. Schweizer, H. Guo, N. Liu, H. Giessen, Synthesis of transmission line models for metamaterial slabs at optical frequencies. *Phys. Rev. B* **78**, 115110 (2008).

44. N. Yu, P. Genevet, M. A. Kats, F. Aieta, J. P. Tetienne, F. Capasso, Z. Gaburro, Light propagation with phase discontinuities: Generalized laws of reflection and refraction. *Science* **334**, 333–337 (2011).
45. V. John, *Antenna Engineering Handbook* (McGraw-Hill Professional, ed. 4, 2007).
46. X. Tu, P. Xiao, L. Kang, C. Jiang, X. Guo, Z. Jiang, R. Su, X. Jia, J. Chen, P. Wu, Nb₅N₆ microbolometer for sensitive, fast-response, 2- μ m detection. *Opt. Express* **26**, 15585–15593 (2018).
47. R. Liu, Q. Wu, M. D. Renzo, Y. Yuan, A path to smart radio environments: An industrial viewpoint on reconfigurable intelligent surfaces. *IEEE Wireless Commun.* **29**, 202–208 (2022).
48. L. Li, Y. Shuang, Q. Ma, H. Li, H. Zhao, M. Wei, C. Liu, C. Hao, C.-W. Qiu, T. J. Cui, Intelligent metasurface imager and recognizer. *Light Sci. Appl.* **8**, 97 (2019).
49. C. Liu, Q. Ma, Z. J. Luo, Q. R. Hong, Q. Xiao, H. C. Zhang, L. Miao, W. M. Yu, Q. Cheng, L. Li, T. J. Cui, A programmable diffractive deep neural network based on a digital-coding metasurface array. *Nat. Electron.* **5**, 113–122 (2022).
50. M. A. Abbas, J. Kim, A. S. Rana, I. Kim, B. Rehman, Z. Ahmad, Y. Massoud, J. Seong, T. Badloe, K. Park, M. Q. Mehmood, M. Zubair, J. Rho, Nanostructured chromium-based broadband absorbers and emitters to realize thermally stable solar thermophotovoltaic systems. *Nanoscale* **14**, 6425–6436 (2022).
51. S. Ariyoshi, C. Otani, A. Dobroiu, H. Sato, K. Kawase, H. M. Shimizu, T. Taino, H. Matsuo, Terahertz imaging with a direct detector based on superconducting tunnel junctions. *Appl. Phys. Lett.* **88**, 203503 (2006).
52. C. Li, J. Wu, S. Jiang, R. Su, C. Zhang, C. Jiang, G. Zhou, B. Jin, L. Kang, W. Xu, J. Chen, P. Wu, Electrical dynamic modulation of THz radiation based on superconducting metamaterials. *Appl. Phys. Lett.* **111**, 092601 (2017).

53. Y. Yang, O. D. Gurbuz, G. M. Rebeiz, An eight-element 370–410-GHz phased-array transmitter in 45-nm CMOS SOI with peak EIRP of 8–8.5 dBm. *IEEE Trans. Microwave Theory Tech.* **64**, 4241–4249 (2016).
54. Y. Tousi, E. Afshari, A high-power and scalable 2-D phased array for terahertz CMOS integrated systems. *IEEE J. Solid-State Circuits* **50**, 597–609 (2015).
55. R. Han, C. Jiang, A. Mostajeran, M. Emadi, H. Aghasi, H. Sherry, A. Cathelin, E. Afshari, A SiGe terahertz heterodyne imaging transmitter With 3.3 mW radiated power and fully-integrated phase-locked loop. *IEEE J. Solid-State Circuits* **50**, 2935–2947 (2015).
56. N. J. Karl, R. W. McKinney, Y. Monnai, R. Mendis, D. M. Mittleman, Frequency-division multiplexing in the terahertz range using a leaky-wave antenna. *Nat. Photonics* **9**, 717–720 (2015).
57. H. Matsumoto, I. Watanabe, A. Kasamatsu, Y. Monnai, Integrated terahertz radar based on leaky-wave coherence tomography. *Nat. Electron.* **3**, 122–129 (2020).
58. Y. Ghasempour, R. Shrestha, A. Charous, E. Knightly, D. M. Mittleman, Single-shot link discovery for terahertz wireless networks. *Nat. Commun.* **11**, 2017 (2020).
59. Z. Chen, X. Chen, L. Tao, K. Chen, M. Long, X. Liu, K. Yan, R. I. Stantchev, E. Pickwell-MacPherson, J.-B. Xu, Graphene controlled Brewster angle device for ultra broadband terahertz modulation. *Nat. Commun.* **9**, 4909 (2018).
60. J. Cai, B. Chen, J. Wu, Y.-H. Li, Q. Xue, T. Wang, C. Zhang, Q. Wen, B. Jin, J. Chen, P. Wu, Reconfigurable terahertz rainbow deflector. *Appl. Phys. Lett.* **118**, 141105 (2021).
61. M. Dyakonov, M. Shur, Detection, mixing, and frequency multiplication of terahertz radiation by two-dimensional electronic fluid. *IEEE Trans. Electron Devices* **43**, 380–387 (1996).

62. J. D. Sun, Y. F. Sun, D. M. Wu, Y. Cai, H. Qin, B. S. Zhang, High-responsivity, low-noise, room-temperature, self-mixing terahertz detector realized using floating antennas on a GaN-based field-effect transistor. *Appl. Phys. Lett.* **100**, 013506 (2012).
63. P. Hillger, J. Grzyb, R. Jain, U. R. Pfeiffer, Terahertz imaging and sensing applications with silicon-based technologies. *IEEE Trans. Terahertz Sci. Technol.* **9**, 1–19 (2019).
64. T. Kleine-Ostmann, P. Dawson, K. Pierz, G. Hein, M. Koch, Room-temperature operation of an electrically driven terahertz modulator. *Appl. Phys. Lett.* **84**, 3555–3557 (2004).
65. Y. Zhang, S. Qiao, S. Liang, Z. Wu, Z. Yang, Z. Feng, H. Sun, Y. Zhou, L. Sun, Z. Chen, X. Zou, B. Zhang, J. Hu, S. Li, Q. Chen, L. Li, G. Xu, Y. Zhao, S. Liu, Gbps terahertz external modulator based on a composite metamaterial with a double-channel heterostructure. *Nano Lett.* **15**, 3501–3506 (2015).
66. S. Venkatesh, X. Lu, H. Saeidi, K. Sengupta, A high-speed programmable and scalable terahertz holographic metasurface based on tiled CMOS chips. *Nat. Electron.* **3**, 785–793 (2020).
67. C. Chen, X. Yi, J. Zhang, X. Zhao, Linear uncooled microbolometer array based on VO_x thin films. *Infrared Phys. Technol.* **42**, 87–90 (2001).
68. S. Vadnala, N. Paul, A. Agrawal, S. G. Singh, Enhanced infrared sensing properties of vanadium pentoxide nanofibers for bolometer application. *Mater. Sci. Semicond. Process.* **81**, 82–88 (2018).
69. X. Chen, X. Yi, VO₂-based microbolometer uncooled infrared focal plane arrays with CMOS readout integrated circuit, in *Asia-Pacific Optical Communications* (SPIE, 2005), vol. 6020 p. 602032.
70. Z. Zhu, P. G. Evans, R. F. Haglund, J. G. Valentine, Dynamically reconfigurable metadvice employing nanostructured phase-change materials. *Nano Lett.* **17**, 4881–4885 (2017).

71. Y. Kim, P. C. Wu, R. Sokhoyan, K. Mauser, R. Glauddell, G. K. Shirmanesh, H. A. Atwater, Phase modulation with electrically tunable vanadium dioxide phase-change metasurfaces. *Nano Lett.* **19**, 3961–3968 (2019).
72. F. H. Koppens, T. Mueller, P. Avouris, A. C. Ferrari, M. S. Vitiello, M. Polini, Photodetectors based on graphene, other two-dimensional materials and hybrid systems. *Nat. Nanotechnol.* **9**, 780–793 (2014).
73. M. S. Ergoktas, G. Bakan, E. Kovalska, L. W. Le Fevre, R. P. Fields, P. Steiner, X. Yu, O. Salihoglu, S. Balci, V. I. Fal'ko, K. Novoselov, R. A. W. Dryfe, C. Kocabas, Multispectral graphene-based electro-optical surfaces with reversible tunability from visible to microwave wavelengths. *Nat. Photonics* **15**, 493–498 (2021).